A MODEL OF THE PULSATILE FLUID FLOW IN THE LYMPH NODE

GIULIA GIANTESIO, ALBERTO GIRELLI, AND ALESSANDRO MUSESTI

Abstract. The aim of the paper is to propose a mathematical model for the flow of the interstitial fluid in a lymph node, which main feature is the presence of a porous bulk region with a very low permeability, surrounded by a thin channel where the fluid can flow freely. The flow is driven by a pulsatile pressure gradient. An explicit solution is found in the case of a laminar flow in a simplified situation, while some finite element simulations are presented in a more realistic geometry.

1. Introduction

A large part of the biomathematical literature is devoted to model the circulatory system (see for instance the review [14] and references therein). However, the focus is almost always on the circulation of blood, while the lymphatic system received much less attention: suffice it to say that [15], one of the first mathematical models of the lymphatic vessels, was published only in 1975. This can be due to the fact that the lymph flows in a non-closed system, consisting of organs, vessels and diverse tissues, making the system very complicated to model.

The primary function of the lymphatic system is to transport excess interstitial fluid from the interstitial space back to the blood circulation, via the thoracic duct. Interstitial fluid (called lymph once inside the lymphatic system) is mainly composed of water which contains sugars, salts, fatty acids, amino acids, coenzymes, hormones, neurotransmitters, white blood cells and cell waste products (it accounts for 26% of the water in the human body). Along with the excess interstitial fluid, excess proteins and waste are transported back to the circulation. The lymphatic system is composed of a network of vessels, capillaries and organs. For a more complete introduction to the lymphatic system, the reader is referred to these reviews [11, 13, 10]. The lymphatic system is an integral part of the immune system thanks to the lymph nodes: they are organs scattered all across the lymphatic network and their function is to filter the lymph and break down bacteria, viruses, and waste. In a nutshell, the two important parts from a fluid dynamic point of view are the lymphoid compartment and its exterior, the subcapsular sinus. The lymphoid compartment is filled with a sponge-like tissue, called reticular meshwork, where the lymph is filtered by macrophages [4]; indeed, certain molecules cannot pass through the external surface and are destroyed by the lymphocytes which are in the lymph nodes. The reticular meshwork contains elongated fibroblastic reticular cells that form an interconnected network, called conduit system [17]; this network contains tubules that are the only entry points for the fluid, forming a labyrinth-like

(G. Giantesio, A. Musesti) Dipartimento di Matematica e Fisica "N. Tartaglia", Università Cattolica del Sacro Cuore, Italy

(A. Girelli) Dipartimento di Matematica e Applicazioni, Università degli Studi di Milano-Bicocca, Italy

E-mail addresses: giulia.giantesio@unicatt.it, a.girelli3@campus.unimib.it, alessandro.musesti@unicatt.it.

Key words and phrases. Lymph node; Pulsatile flow; Darcy–Brinkman equation.

structure. It seems natural to model such a tissue as a porous medium. On the contrary, the part outside the lymphoid compartment (inside the subcapsular sinus) is a non-porous body, and here the lymph is not filtered. Lymph nodes present a relatively high resistance to flow; due to this, most of the lymph exits the node from the efferent lymphatics without entering the lymphoid compartment [7, 10].

From a mathematical point of view, there are a lot of models that try to describe the behavior of different cell processes and that use some data-driven and computational technique to describe the fibroblast reticular cells and the blood vessels network organization inside the node [12, 18]; but, despite the importance of fluid flow and the mechanics of the lymph node [1, 13, 6, 19], from a continuum mechanics point of view the models are in their infancy [2, 3, 7, 5, 8] and are primarily oriented to a physiological description instead of a more mechanical one. Hence the aim of this paper is to propose a simple model of the circulation of lymphatic fluid in a lymph node.

Our model is very idealized and is a starting point for more advanced studies on the subject. To begin with, we assume that the lymph node is essentially composed of two parts: a porous medium, modeling the lymphoid compartment, characterized by a permeability constant K, surrounded by a thin channel in which the lymph can flow freely. We describe the motion of the interstitial fluid within the lymph node using the Darcy–Brinkman equation in the porous core and the Navier–Stokes equation in the external channel. Differently from other studies present in the literature [7, 3], here the motion is induced by a pulsatile gradient of pressure, so that it has to be non-stationary. Being the lymph composed mainly of water, as usual, we assume the incompressibility of the fluid.

2. Solving the problem in a very simplified geometry

As mentioned in the previous section, the geometry of a lymph node is very complex. To begin with, we will assume a much more simplified geometry, so that we can find an explicit expression for the solution even in the presence of a pulsatile pressure gradient. More precisely, the lymph node is here represented by a cylinder and it is permeated by an incompressible homogeneous Newtonian fluid. The incompressibility constraint is motivated by the fact that the interstitial fluid is essentially a water solvent.

The region $r \in [0, R_1]$ represents the lymphoid compartment (LC). For simplicity, we assume that the boundaries do not perform any contraction. This assumption is motivated by the fact that the contractions of the boundaries of the lymph node have a very long period with respect to the pressure gradient [20].

We treat the part of the lymph inside the LC as a porous medium, describing the flow by the Darcy–Brinkman equation, while outside the LC we use the Navier–Stokes equation. Hence, the flow of the fluid in the absence of body forces is governed by

$$\rho_0 \frac{\partial \boldsymbol{v}}{\partial t} + \rho_0 (\operatorname{grad} \boldsymbol{v})\boldsymbol{v} = -\operatorname{grad} p - \frac{\mu}{K}\boldsymbol{v} + \mu \Delta \boldsymbol{v} \tag{1}$$

for $r \in [0, R_1]$ (inside the LC) and by

$$\rho_0 \frac{\partial \boldsymbol{v}}{\partial t} + \rho_0 (\operatorname{grad} \boldsymbol{v})\boldsymbol{v} = -\operatorname{grad} p + \mu \Delta \boldsymbol{v} \tag{2}$$

for $r \in (R_1, R_2]$ (outside the LC), together with the incompressibility constraint $\operatorname{div} \boldsymbol{v} = 0$. Here ρ_0 is the constant density of the lymph, μ the constant viscosity, K the permeability of the LC and $\boldsymbol{v}$ and p are the velocity and the pressure field of the lymph, respectively.

Thanks to the symmetry of this idealized problem, we look for a laminar velocity field of the form

$$\boldsymbol{v} = v_z(r,t)\boldsymbol{e}_z,$$

where $\boldsymbol{e}_z$ is the axis of the cylinder and r the radial coordinate. In particular, the incompressibility constraint $\operatorname{div} \boldsymbol{v} = 0$ is automatically satisfied.

Notice that the laminarity assumption is quite restrictive, especially because it prevents any flow of the fluid from the LC to the external region, and *vice versa*. Such a flow, which can be very important, will be recovered in the numerical simulations of 4.

As far as the boundary and initial conditions are concerned, we assume:

$$v_z(R_2,t) = 0 \text{ (no-slip condition)}, \tag{3}$$

$$v_z(0,t) \text{ bounded}, \tag{4}$$

$$v_z \in C^1 \text{ (smoothness condition)}, \tag{5}$$

$$v_z(r,0) = v_{z0}(r) \text{ (initial condition)}. \tag{6}$$

Then, Eqs. $(1)_1$ and $(2)_1$ reduce to

$$\frac{\partial v_z}{\partial t} - \nu \frac{1}{r}\frac{\partial}{\partial r}\left(r\frac{\partial v_z}{\partial r}\right) + \chi_{[0,R_1]}\frac{\nu}{K}v_z = g(t) \tag{7}$$

where we put $-\frac{1}{\rho_0}\frac{\partial p}{\partial z} = g(t)$ and $\nu = \mu/\rho_0$, and the *characteristic function of a set* A is defined as $\chi_A(x) = 1$ if $x \in A$ and $\chi_A(x) = 0$ elsewhere.

Denoting with $v_z^{(1)}$ the solution in $[0, R_1]$ and with $v_z^{(2)}$ the solution in $(R_1, R_2]$, the smoothness condition (5) implies that, for every t:

$$v_z^{(1)}(R_1,t) = v_z^{(2)}(R_1,t), \quad \frac{\partial v_z^{(1)}}{\partial r}(R_1,t) = \frac{\partial v_z^{(2)}}{\partial r}(R_1,t).$$

The problem writes as a linear PDE in the form

$$\frac{1}{\nu}\frac{\partial v_z}{\partial t} + Lv_z = \frac{1}{\nu}g(t), \tag{8}$$

where

$$Lu = -\frac{1}{r}\frac{\partial}{\partial r}\left(r\frac{\partial u}{\partial r}\right) + \chi_{[0,R_1]}\frac{1}{K}u \tag{9}$$

is a linear operator. Hence it is useful to characterize the eigenvalues (λ_k) and the eigenfunctions (ϕ_k) of the operator L,

$$L\phi_k = \lambda_k \phi_k,$$

where $\phi_k(r)$ has to be bounded as $r \to 0^+$, $\phi_k(r)$ and $\phi_k'(r)$ continuous for $r = R_1$, and $\phi_k(R_2) = 0$, for all values of k.

2.1. **Eigenvalues of the linear operator.** It is easy to prove that the eigenvalues λ_k are positive; however it is convenient to consider the two cases $\lambda_k < 1/K$ and $\lambda_k \geq 1/K$. Since by a standard change of variables the equation $L\phi_k = \lambda_k\phi_k$ can be put in the form of a Bessel equation with $\nu = 0$, then the eigenfunctions can be written as a linear combination of J_0 and Y_0, the Bessel functions of order 0 of the first and second kind, respectively:

$$\phi_k(r) := \begin{cases} \bar{A}_k J_0\left(r\sqrt{\lambda_k - \frac{1}{K}}\right) + \bar{B}_k Y_0\left(r\sqrt{\lambda_k - \frac{1}{K}}\right) & r \in [0, R_1] \\ A_k J_0\left(r\sqrt{\lambda_k}\right) + B_k Y_0\left(r\sqrt{\lambda_k}\right) & r \in (R_1, R_2]. \end{cases} \tag{10}$$

Notice that in the case $\lambda_k < 1/K$ the argument of the Bessel functions in the first case is imaginary, hence we can rewrite it as

$$\bar{A}_k I_0\left(r\sqrt{\frac{1}{K}-\lambda_k}\right)+\bar{B}_k K_0\left(r\sqrt{\frac{1}{K}-\lambda_k}\right) \quad r\in[0,R_1],$$

by using the *modified* Bessel functions I_0, K_0.

Now we impose the boundedness at $r=0$, the smoothness at $r=R_1$ and the vanishing boundary condition at $r=R_2$. Since Y_0 and K_0 are unbounded in the origin, we must impose $\bar{B}_k=0$, obtaining the following linear system:

$$\begin{cases} \bar{A}_k J_0\left(R_1\sqrt{\lambda_k-\frac{1}{K}}\right)-A_k J_0\left(R_1\sqrt{\lambda_k}\right)-B_k Y_0\left(R_1\sqrt{\lambda_k}\right)=0 \\ -\bar{A}_k\sqrt{\lambda_k-\frac{1}{K}}J_1\left(R_1\sqrt{\lambda_k-\frac{1}{K}}\right)+A_k\sqrt{\lambda_k}J_1\left(R_1\sqrt{\lambda_k}\right) \\ \qquad +B_k\sqrt{\lambda_k}Y_1\left(R_1\sqrt{\lambda_k}\right)=0 \\ A_k J_0\left(R_2\sqrt{\lambda_k}\right)+B_k Y_0\left(R_2\sqrt{\lambda_k}\right)=0 \end{cases} \tag{11}$$

where we should replace J_0, J_1 with $I_0, -I_1$, respectively, in the case $\lambda_k < 1/K$. The first two equations in (11) come from the smoothness at R_1 and the last equation from the boundary condition (and we used the fact that $J_0'=-J_1$, $Y_0'=-Y_1$ and $I_0'=I_1$). Then the eigenvalues of the linear operator L defined in (9) can be found imposing that the linear system (11) has nontrivial solutions, that is $\det \mathsf{A}=0$, where A is the 3×3 matrix of the linear system in the unknowns $\bar{A}_k, A_k, B_k$. One can prove that there is an increasing unbounded sequence (λ_k) of simple zeros of the equation. Then, for every eigenvalue λ_k one can solve the linear system (11), finding the coefficients $\bar{A}_k, A_k, B_k$ and hence the corresponding eigenfunction ϕ_k (10), up to a multiplicative factor.

2.2. **Orthogonality of the eigenfunctions.** By standard methods one can prove that two eigenfunctions ϕ_k, ϕ_h defined in (10), corresponding to different eigenvalues λ_k, λ_h, are orthogonal with respect to the weighted scalar product in L^2 (keeping in mind that r is the radial coordinate), namely:

$$\lambda_k \neq \lambda_h \quad \Rightarrow \quad \int_0^{R_2} r\phi_k(r)\phi_h(r)\,dr=0.$$

Indeed, the two eigenfunctions satisfy the equations

$$r\frac{\partial^2\phi_j}{\partial r^2}+\frac{\partial\phi_j}{\partial r}-r\chi_{[0,R_1]}\frac{1}{K}\phi_j+r\lambda_j\phi_j=0, \quad j=h,k.$$

Multiplying one equation by ϕ_h and the other by ϕ_k and taking the difference, we get

$$\frac{\partial}{\partial r}\left(r\Big(\phi_h\frac{\partial\phi_k}{\partial r}-\phi_k\frac{\partial\phi_h}{\partial r}\Big)\right)=(\lambda_h-\lambda_k)r\phi_k\phi_h.$$

Integrating between 0 and R_2 and keeping into account that $\phi_k(R_2)=\phi_h(R_2)=0$, we obtain

$$(\lambda_k-\lambda_h)\int_0^{R_2} r\phi_k(r)\phi_h(r)\,dr=0,$$

which gives the orthogonality whenever $\lambda_k \neq \lambda_h$. Moreover, following [21, (10) p. 134] one can prove that

$$\begin{aligned}\int_0^{R_2} r\phi_k^2(r)\,dr &= \frac{R_1^2}{2K\lambda_k}\left[\bar{A}_k J_1\Big(R_1\sqrt{\lambda_k-\frac{1}{K}}\Big)\right]^2 \\ &\quad +\frac{R_2^2}{2}\left[A_k J_1\left(R_2\sqrt{\lambda_k}\right)+B_k Y_1\left(R_2\sqrt{\lambda_k}\right)\right]^2\end{aligned}$$

in case $\lambda_k \geq 1/K$, and

$$\begin{aligned}\int_0^{R_2} r\phi_k^2(r)\,dr &= -\frac{R_1^2}{2K\lambda_k}\left[\bar{A}_k I_1\Big(R_1\sqrt{\frac{1}{K}-\lambda_k}\Big)\right]^2 \\ &\quad +\frac{R_2^2}{2}\left[A_k J_1\left(R_2\sqrt{\lambda_k}\right)+B_k Y_1\left(R_2\sqrt{\lambda_k}\right)\right]^2\end{aligned}$$

in case $\lambda_k < 1/K$. Dividing by the norm, it is not restrictive to assume that the sequence of eigenfunctions is *normalized*, that is

$$\int_0^{R_2} r\phi_k^2(r)\,dr = 1.$$

2.3. **Fourier coefficients and long-time behavior.** In order to give an explicit form of the solution of the PDE (8), let us introduce the Fourier coefficients

$$c_k := \int_0^{R_2} r\phi_k(r)\,dr, \quad \sum_{k=1}^{\infty} c_k\phi_k(r) = 1.$$

By using the formula (see [21, (1) p. 132])

$$\int rZ_0(r)\,dr = rZ_1(r), \quad Z = J, Y, I$$

one can prove that

$$\begin{aligned}c_k &= \frac{R_1\bar{A}_k}{K\lambda_k\sqrt{\left|\lambda_k-\frac{1}{K}\right|}}Z\Big(R_1\sqrt{\Big|\lambda_k-\frac{1}{K}\Big|}\Big) \\ &\quad +\frac{R_2}{\sqrt{\lambda_k}}\left[A_k J_1\left(R_2\sqrt{\lambda_k}\right)+B_k Y_1\left(R_2\sqrt{\lambda_k}\right)\right]\end{aligned}$$

where $Z = J_1$ in case $\lambda_k \geq 1/K$ and $Z = I_1$ in case $\lambda_k < 1/K$.

Taking the solution in the form

$$v_z(r,t) = \sum_{k=1}^{\infty} v_k(t)\phi_k(r),$$

we can rewrite (8) as

$$\frac{1}{\nu}\sum_{k=1}^{\infty} v_k'(t)\phi_k(r) + \sum_{k=1}^{\infty}\lambda_k v_k(t)\phi_k(r) = \frac{g(t)}{\nu}\sum_{k=1}^{\infty} c_k\phi_k(r).$$

Multiplying by $r\phi_k(r)$ and integrating on $[0, R_2]$, we find the sequence of ODEs

$$\frac{1}{\nu}v_k'(t) + \lambda_k v_k(t) = \frac{c_k}{\nu}g(t), \qquad k \geq 1,$$

which can be easily solved:

$$v_k(t) = e^{-\nu\lambda_k t}\left(v_k(0) + c_k\int_0^t e^{\nu\lambda_k\tau}g(\tau)\,d\tau\right).$$

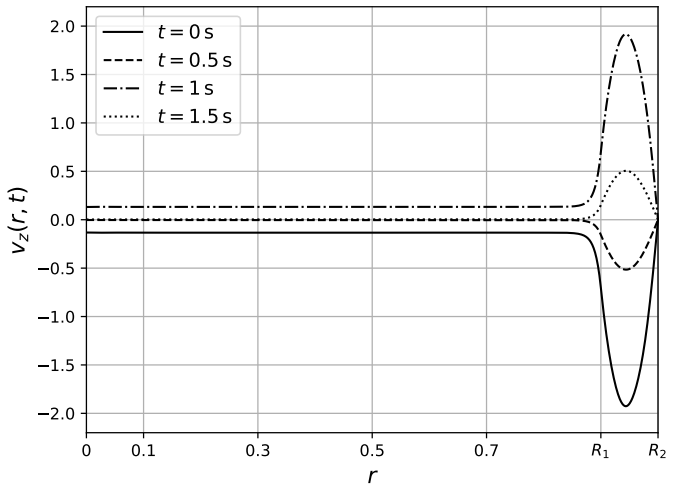

FIGURE 1. The long-time behavior of the solution. The parameters are given in 1.

The coefficients $v_k(0)$ can be computed by writing the Fourier coefficients of the initial datum

$$v_z(r,0) = v_{z0}(r), \quad r \in [0, R_2],$$

that is

$$v_k(0) = \int_0^{R_2} v_{z0}(r)\phi_k(r)\,dr, \quad \sum_{k=1}^{\infty} v_k(0)\phi_k(r) = v_{z0}(r).$$

Since $\lambda_k > 0$, it is easy to see that for $t \to +\infty$ one has

$$v_k(t) \approx e^{-\nu\lambda_k t} c_k \int_0^t e^{\nu\lambda_k \tau} g(\tau)\,d\tau,$$

hence the long-time behavior of the solution does not depend on the initial datum.

As an example, let us consider a harmonic pulsatile pressure gradient of the form

$$\frac{\partial p}{\partial z} = C + G\cos\omega t, \quad g(t) = -\frac{1}{\rho_0}(C + G\cos\omega t) \tag{12}$$

where C is the pressure drop of the basic flow and the constants G, ω determine the pulsatility of the motion. Then one can explicitly compute the Fourier coefficients for the long-time behavior:

$$v_k(t) \approx -\frac{G\nu\lambda_k\omega\sin\omega t + G\nu^2\lambda_k^2\cos\omega t + C\omega^2 + C\nu^2\lambda_k^2}{\nu\lambda_k\rho_0(\omega^2 + \nu^2\lambda_k^2)}.$$

The long-time solution then behaves as

$$-\sum_{k=1}^{\infty} \frac{G\nu\lambda_k\omega\sin\omega t + G\nu^2\lambda_k^2\cos\omega t + C\omega^2 + C\nu^2\lambda_k^2}{\nu\lambda_k\rho_0(\omega^2 + \nu^2\lambda_k^2)}\phi_k(r),$$

which is represented in 1. We used the first 40 eigenfunctions: by increasing that number, the plot does not change appreciably. We can notice a periodic profile with a period of 2 s.

3. The explicit expression of the long-time solution

In this section, we give an explicit form of the long-time periodic solution of the problem. Actually, we look for an explicit solution of (7) of the form

$$v_z(r,t) = v_p(r) + Re\left(U(r)e^{i\omega t}\right), \tag{13}$$

where $U(r)$ has to be determined and v_p is the velocity of the Poiseuille part of the flow.

We recall that the Poiseuille flow refers to the steady laminar solution of problem (1)–(2). Hence we search a solution $\boldsymbol{v} = v_p(r)\boldsymbol{e}_z$ of

$$-\nu\frac{1}{r}\frac{\partial}{\partial r}\left(r\frac{\partial v_p}{\partial r}\right) + \chi_{[0,R_1]}\frac{\nu}{K}v_p = -\frac{1}{\rho_0}C, \tag{14}$$

where C is the pressure drop in z-direction.

After some calculations, we get

$$v_p(r) = \begin{cases} Re\left(-\dfrac{C}{\mu}K + c_5 J_0(\xi_p)\right) & r \in [0,R_1], \\ Re\left(\dfrac{C}{4\mu}r^2 + c_6\log r + c_7\right) & r \in (R_1,R_2], \end{cases} \tag{15}$$

where J_0 is the Bessel functions of order 0 of the first kind, $\xi_p(r) = ir/\sqrt{K}$ and c_5, c_6, c_7 are obtained by the boundary conditions

$$v_p(R_2) = 0, \quad v_p(0) \text{ bounded}, \quad v_p \in C^1.$$

We now put (13) in (7) and simplify the exponential part, obtaining

$$U''(r) + \frac{1}{r}U'(r) - \left(\chi_{[0,R_1]}\frac{1}{K} + \frac{i\rho_0\omega}{\mu}\right)U(r) = \frac{G}{\mu},$$

which is a second order ODE in the form of a Bessel equation. Hence, its solution can be written in the form:

$$U(r) = \begin{cases} -\dfrac{GK}{\mu + i\rho_0\omega K} + \bar{A}J_0(\xi_K(r)) + \bar{B}Y_0(\xi_K(r)) & r \in [0,R_1], \\ \dfrac{iG}{\omega\rho_0} + AJ_0(\xi(r)) + BY_0(\xi(r)) & r \in (R_1,R_2], \end{cases}$$

where J_0 and Y_0 are Bessel functions of the first and second kind and ξ_K, ξ are complex variables related to the radius r:

$$\xi_K(r) = i\sqrt{\frac{1}{K} + \frac{i\omega\rho_0}{\mu}}r, \qquad \xi(r) = \frac{i-1}{\sqrt{2}}\sqrt{\frac{\omega\rho_0}{\mu}}r. \tag{16}$$

The constants $\bar{A}$, $\bar{B}$, A and B have to be determined using the boundary conditions.

From the no-slip condition (3), we have

$$U(R_2) = 0 \quad \Rightarrow \quad \frac{iG}{\omega\rho_0} + AJ_0(\xi(R_2)) + BY_0(\xi(R_2)) = 0,$$

while the boundedness in $r = 0$ (4) gives $\bar{B} = 0$.

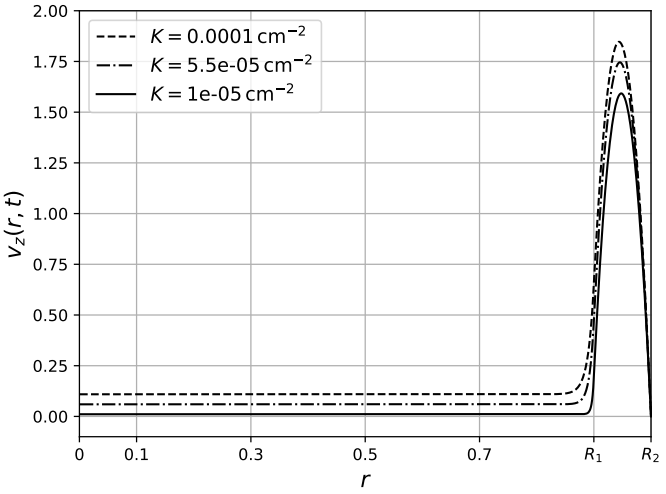

FIGURE 2. Trend of the velocity when K varies at $t = 1.2\,\mathrm{s}$. The values of the parameters not explicitly mentioned in the figure are given in 1.

Finally, we impose condition (5) and after some calculations we get

$$\begin{aligned}
\Xi =& \frac{\xi_K'(r)}{\xi'(r)} = \frac{\sqrt{2}}{2}(1-i)\sqrt{\frac{\mu + iK\rho_0\omega}{K\rho_0\omega}},\\
d =& J_0(\xi(R_2))Y_1(\xi(R_1)) - Y_0(\xi(R_2))J_1(\xi(R_1)),\\
f =& J_0(\xi(R_2))Y_0(\xi(R_1)) - Y_0(\xi(R_2))J_0(\xi(R_1)),\\
A =& -\frac{iG}{\omega\rho_0}\frac{Y_1(\xi(R_1))}{d} - \Xi\bar{A}\frac{Y_0(\xi(R_2))J_1(\xi_K(R_1))}{d},\\
B =& \frac{iG}{\omega\rho_0}\frac{J_1(\xi(R_1))}{d} + \Xi\bar{A}\frac{J_0(\xi(R_2))J_1(\xi_K(R_1))}{d},\\
\bar{A} =& \frac{iG}{\omega\rho_0}\frac{-d + Y_1(\xi(R_1))J_0(\xi(R_1)) - J_1(\xi(R_1))Y_0(\xi(R_1))}{\Xi J_1(\xi_K(R_1))f - J_0(\xi_K(R_1))d}\\
&- \frac{GK}{\mu + iK\rho_0\omega}\frac{d}{\Xi J_1(\xi_K(R_1))f - J_0(\xi_K(R_1))d}.
\end{aligned}$$

Plotting the solution (13) we obtain again the results of 1. In 2 we show the velocity profile at a fixed time for some values of the permeability K.

4. Numerical solutions in more complex geometries

In this section, we perform some numerical simulations of the full two-dimensional problem with Finite Elements using FreeFem++. We use the classical weak formulation for both the Darcy–Brinkman and the Navier–Stokes equations.

Let us define the *resistivity*

$$r^* = \begin{cases} 1/K & \text{inside LC} \\ 0 & \text{outside LC} \end{cases}$$

which is implemented as a finite element function (so that at the interface between the LC and the subcapsular sinus, r^* is connected with continuity).

TABLE 1. Numerical values of the parameters related to the physical quantities of the lymph node [2].

R_1	$0.9\,\mathrm{cm}$
R_2	$1\,\mathrm{cm}$
ρ_0	$1\,\mathrm{g\,cm^{-3}}$
μ	$0.015\,\mathrm{g\,cm^{-1}\,s^{-1}}$
C	$0.05\,\mathrm{g\,cm^{-2}\,s^{-2}}$
G	$20\,\mathrm{g\,cm^{-2}\,s^{-2}}$
ω	π
K	$10^{-4}\,\mathrm{cm^2}$

For the spatial discretization, we use the finite element space $\mathbb{P}_h^2 = \{\boldsymbol{w} \in \mathbb{H}^1(\Omega) | \forall \mathcal{K} \in T_h, \boldsymbol{w}_{|\mathcal{K}} \in P_2\}$ for the velocity, and $\mathbb{P}_h^1 = \{q \in \mathbb{H}^1(\Omega) | \forall \mathcal{K} \in T_h, q_{|\mathcal{K}} \in P_1\}$ for the pressure; these choices guarantee us the inf–sup stability. For the time discretization, we use the BDF2 method. Moreover, we use a grad-div stabilization (see [16]), Newton's method for matrix and GMRES as solver, with the same parameters given in 1.

4.1. **The cylindrical case.** First of all, we study a cylindrical domain with length L and external radius R_2, where the LC is an inner coaxial cylinder with radius R_1. Using cylindrical coordinates, we assume axial symmetry and $v_\theta = 0$, so that we can consider a rectangular mesh $[0, R_2] \times [0, L]$. Notice that the resistivity r^* is different from zero only in the LC, which is described by the rectangle $[0, R_1] \times [0, L]$. Denoting as usual by v_r and v_z the radial and axial components of the velocity, respectively, the boundary and initial conditions are: $\boldsymbol{v}(R_2, z, t) = \mathbf{0}$ (no-slip condition in R_2), $v_r(0, z, t) = 0$ (symmetry condition), $\frac{\partial v_z}{\partial r}(0, z, t) = 0$ (homogeneous Neumann b.c. in $r = 0$), $\frac{\partial \boldsymbol{v}}{\partial z}(r, 0, t) = \frac{\partial \boldsymbol{v}}{\partial z}(r, L, t) = \mathbf{0}$ (homogeneous Neumann b.c. in $z = 0$ and in $z = L$), $\boldsymbol{v}(r, z, 0) = \mathbf{0}$ for $z \in (0, R_2]$ (fluid initially at rest).

Moreover we impose the inlet condition

$$v_z(r, 0, t) = \left[\frac{C}{4\mu} \left(R_2^2 - r^2 \right) + Re \left(e^{i\omega t} \frac{iG}{\omega \rho_0} \left(1 - \frac{J_0(\xi(r))}{J_0(\xi(R_2))} \right) \right) \right]^+ \tag{17}$$

where $[\,]^+$ is the positive part and $\xi(r)$ is given in (16). This is a pulsatile Poiseuille flow truncated with a positive part; the aim of this function is to model the valve behavior at the end of the lymphangion, which prevents retrograde flows [9, 15].

We plot the simulations at a large time, in order to reach the periodicity of the solution, the period being $T = 2\,\mathrm{s}$. 3 shows the axial component of the velocity vector field at three different values of z: as the coordinate z increases, the porous part tends to slow down the flow in the LC.

In 4–5 we plot the two components of the velocity field at $z = 0.5\,\mathrm{cm}$ for some values of t. In particular, 5 shows that there is a non negligible radial component of the velocity, so that the flow is far from being laminar. Hence the theoretical results of 2–3 are not comparable with this simulation.

4.2. **The spheroidal case.** Now we numerically study the same problem in a more complex and realistic geometry, that is an oblate spheroid [7]. We suppose that the velocity does not depend on the angle θ, hence we can consider a half-ellipse defined by the parametric equations

$$x = r \cos\phi, \quad y = 0.5 r \sin\phi, \qquad r \in [0, R_2],\ \phi \in \left[-\frac{\pi}{2}, \frac{\pi}{2} \right],$$

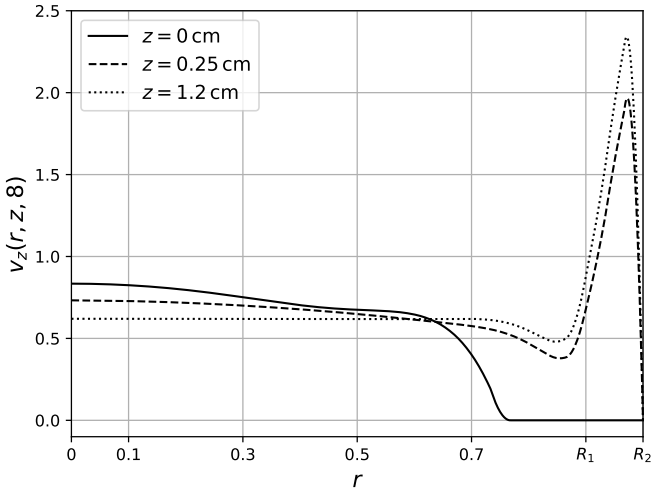

FIGURE 3. Cylindrical case: axial velocity profile with respect to r for different values of z at a fixed time $t = 8\,\mathrm{s}$.

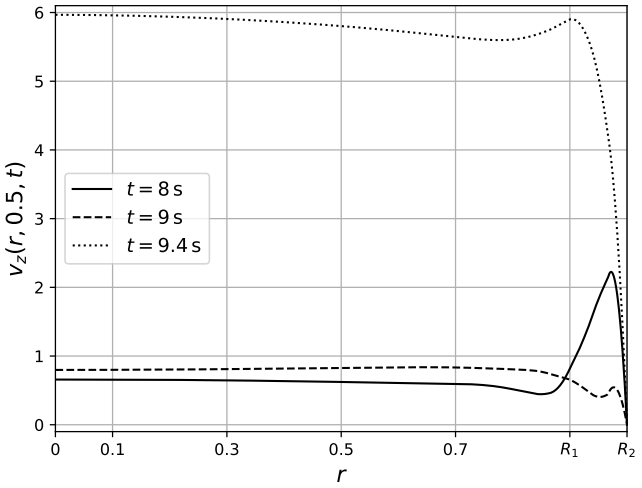

FIGURE 4. Cylindrical case: the component v_z of the velocity at $z = 0.5$ for some values of t.

obtaining the oblate spheroid with a rotation around the $x = 0$ axis. The LC is the smaller spheroid

$$x^2/(0.9)^2 + y^2/(0.4)^2 < 1,$$

hence r^* vanishes outside the smaller spheroid.

We plot the numerical solution in 6. The inlet condition is given by (17) for $\phi \in [-\frac{\pi}{2}, -\frac{\pi}{3}]$ (black boundary). In the outlet part $\phi \in [\frac{\pi}{3}, \frac{\pi}{2}]$ (green boundary) we impose the homogeneous Neumann boundary condition. Moreover, we impose the no-slip condition for $\phi \in [-\frac{\pi}{3}, \frac{\pi}{3}]$ (red boundary), and $v_r = 0$ and homogeneous Neumann b.c. in $\phi = \pm\frac{\pi}{2}$, $r \in [0, R_2]$ (blue boundary).

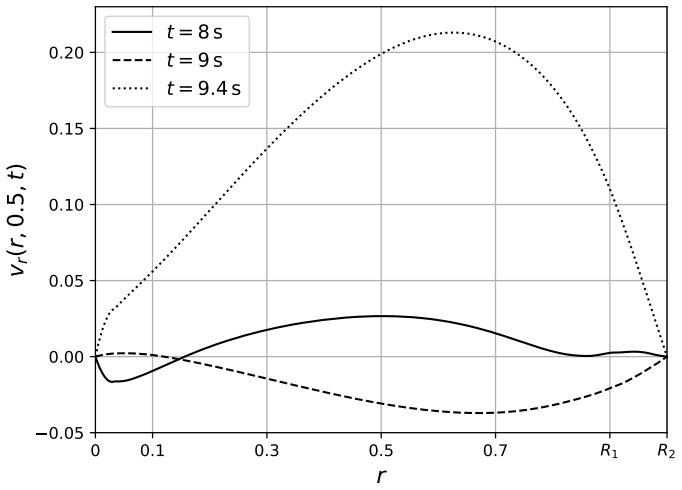

FIGURE 5. Cylindrical case: the component v_r of the velocity at $z = 0.5$ for some values of t.

We plot the results for $t = 1.5\,\mathrm{s}$, when the velocity is maximal. The behavior of the simulation over time is similar to the case of a cylinder. If we decrease the permeability K, the fluid in the LC tends to flow in the non-porous zone outside the smaller spheroid, as one can see in 6_2, where we take $K = 10^{-6}$ cm^2. This is the reason why the majority of the lymph flows outside the node without getting filtered by the lymphoid compartment: indeed, from the incompressibility of the lymph we have that, if we decrease the permeability K, the velocity of the lymph inside the porous part decreases and, to accommodate that, the lymph that flows in the non-porous part outside LC increases its velocity. When there are pathogens in the lymph, the lymph node increases its dimensions and its permeability; apparently, in this way a greater part of the lymph enters in the lymphoid compartment and can be filtered.

We notice that the time dependence of the solution is important for the study of the lymph behavior inside the node. Indeed, in the lymph node the fluid keeps oscillating between moments of almost rest to moments of flowing pumped by a combination of lymphangion contractions and valve disclosures. In our model, when the positive part of the inlet condition is non zero, the lymph enters the lymph node and, when the inlet condition becomes zero, the lymph moves with a very low velocity.

To conclude, we can say that the pulsatile behavior and the presence of a non porous region outside the LC have an important role for the transport of the lymph in the lymph node. We also performed some simulations where we decrease the dimension of the region outside the LC, which we do not show for the sake of brevity; as one would expect, the lymph increases its maximum velocity in the external part as the size of the region decreases. We remark that we did not find any data in the literature regarding the proportion between the LC and the external part; in any case, the maximum of the velocity is always reached outside the LC, whatever the dimension of the two parts, provided that the non porous part is much smaller than the LC.

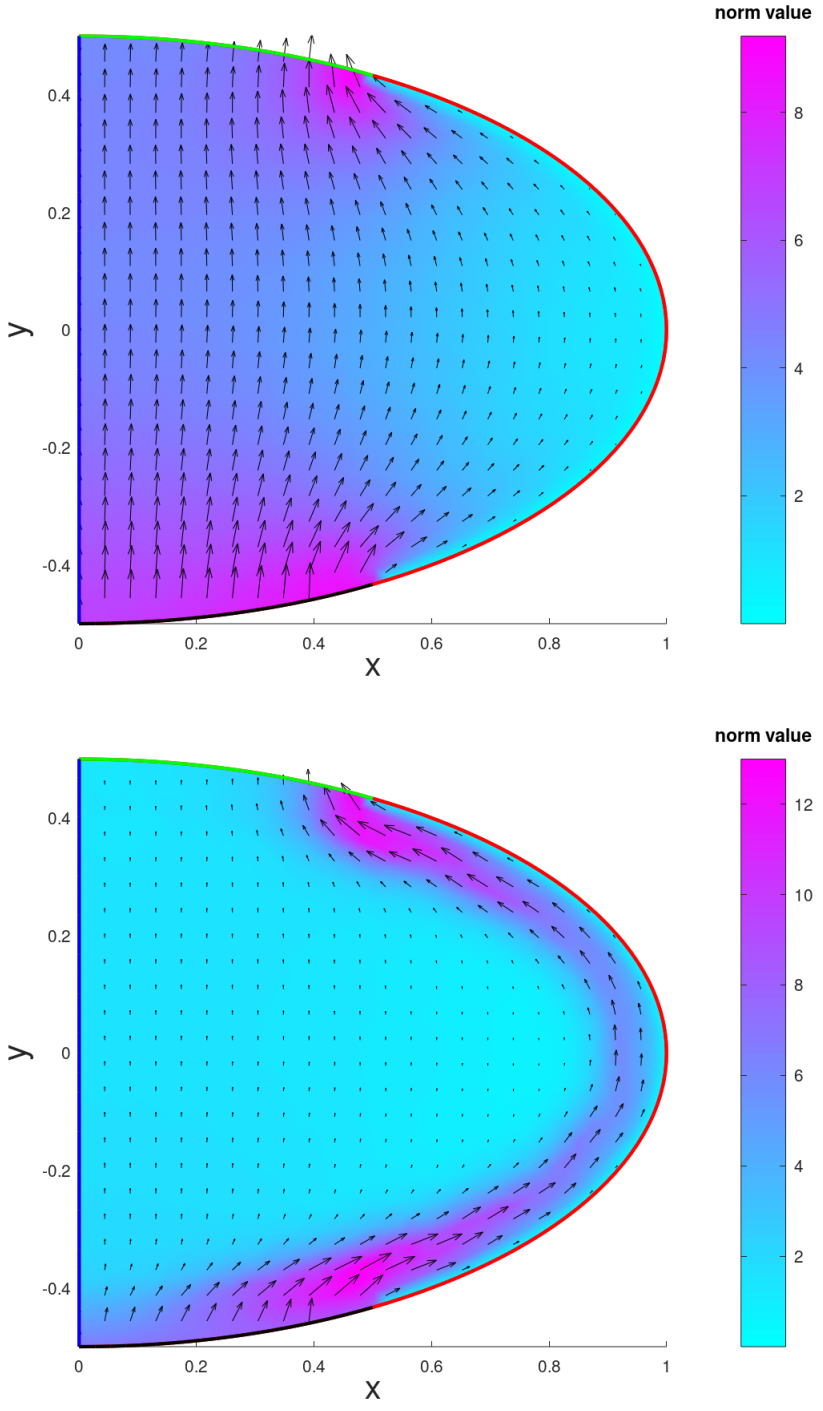

FIGURE 6. Spheroidal case: velocity vector and its norm at the fixed time $t = 1.5\,\mathrm{s}$, for $K = 10^{-4}\ \mathrm{cm}^2$ and $K = 10^{-6}\ \mathrm{cm}^2$, resp.

5. Conclusions

Motivated by the scarcity of papers in the literature on the modeling of the lymphatic system, we have studied the flow of the interstitial fluid in a lymph node. The lymph node is here assumed to be essentially composed by a porous core, where the fluid is governed by the Darcy–Brinkman equation, and a thin layer in which the lymph can flow freely following the Navier–Stokes equation. In the first part of the paper, we further assume laminarity, so that we can get an explicit solution in terms of Bessel functions. Then, we perform some finite element simulations to allow the exchange of flow between the porous and non-porous part, finding that the hypothesis of laminarity is too restrictive in this case. Both the exact solution and the numerical simulations show that the porous part slows the motion; as expected, this behavior explains why the majority of the lymph entering the lymph node does not enter the LC [10]. We can also expect, in response of some pathology, the lymph node to change its dimension in order to increase the permeability K and the proportion between the LC and the non porous part, allowing the lymph node to filter more fluid than usual. We remark that our results are qualitative: the material parameters here are chosen according to [2] and they do not come from any medical or experimental data.

Possible future directions are the validation of the model by means of experimental data and the implementation of more realistic geometries where several porous and non-porous parts interact. Moreover, in the finite element simulations the flow is induced by (17), which describes the valves behavior with an inlet Poiseuille flow. One interesting improvement of the model could be considering the behavior of the lymphangion and the fluid exchange with the blood vessel.

Acknowledgement

This work was partially supported by National Group of Mathematical Physics (GNFM-INdAM), Italy.

References

[1] F. Apoorva, A. M. Loiben, S.B. Shah, A. Purwada, L. Fontan, R. Goldstein, B. J. Kirby, A. M. Melnick, B. D. Cosgrove, and A. Singh. How biophysical forces regulate human B cell lymphomas. *Cell Reports*, 23:499–511, 2018.

[2] L. J. Cooper, J. P. Heppell, G. F. Clough, B. Ganapathisubramani, and T. Roose. An image-based model of fluid flow through lymph nodes. *Bulletin of Mathematical Biology*, 78:52–71, 2015.

[3] L. J. Cooper, B. Zeller-Plumhoffl, G. F. Clough, B. Ganapathisubramani, and T. Roose. Using high resolution X-ray computed tomography to create an image based model of a lymph node. *Journal of Theoretical Biology*, 449:73–82, 2018.

[4] C. L. Willard-Mack. Normal structure, function, and histology of lymph nodes. *Toxicologic Pathology*, 34(4):409–424, 2006.

[5] D. Grebennikov, R. van Loon, M. Novkovic, L. Onder, R. Savinkov, I. Sazonov, R. Tretyakova, W. J. Watson, and G. Bocharov. Critical issues in modelling lymph node physiology. *Computation*, 5(1), 2017.

[6] M. Jafarnejad, D. C. Jawieja, B. S. Brook, R. J. B. Nibbs, and J. E. Jr. Moore. A novel computational model predicts key regulators of chemokine gradient formation in lymph nodes and site-specific roles for CCL19 and ACKr4. *The Journal of Immunology*, 199(7):2291–2394, 2017.

[7] M. Jafarnejad, M. C. Woodruff, D. C. Zawieja, M.C. Carroll, and J. E. Moore Jr. Modeling lymph flow and fluid exchange with blood vessels in lymph nodes. *Lymphatic Research and Biology*, 13(4):234–247, 2015.

[8] S. Jamalian, M. J. Davis, D. C. Zawieja, and J. E. Jr. Moore. Network scale modeling of lymph transport and its effective pumping parameters. *PLOS ONE*, 11(2), 2016.

[9] A. J. Macdonald, K. P. Arkill, G. R. Tabor, N. G. McHale, and C. P. Winlove. Modeling flow in collecting lymphatic vessels: one-dimensional flow through a series of contractile elements. *American Journal of Physiology-Heart and Circulatory Physiology*, 295(1):H305–H313, 2008.

[10] K.N. Margaris and R.A. Black. Modelling the lymphatic system: challenges and opportunities. *Journal of the Royal Society, Interface*, 9(69):601–612, 2012.

[11] A. Mozokhina and R. Savinkov. Mathematical modelling of the structure and function of the lymphatic system. *Mathematics*, 8(9), 2020.

[12] M. Novkovic, L. Onder, H. W. Cheng, G. Bocharov, and B. Ludewig. Integrative computational modeling of the lymph node stromal cell landscape. *Front. Immunol.*, 9(2428), 2018.

[13] M. J. O'Melia, A. W. Lund, and A. N. Thomas. The biophysics of lymphatic transport: Engineering tools and immunological consequences. *iScience*, 22:28–43, 2019.

[14] A. Quarteroni, A. Manzoni, and C. Vergara. The cardiovascular system: Mathematical modelling, numerical algorithms and clinical applications. *Acta Numerica*, 26:365–590, 2017.

[15] N.P. Reddy, T. A. Krouskop, and P. H. Newell. Biomechanics of a lymphatic vessel. *Blood Vessels*, 12(5):261–278, 1975.

[16] Y. Rong and J. Fiordilino. Numerical analysis of a BDF2 modular grad-div stabilization method for the Navier-Stokes equations. *Journal of Scientific Computing*, 82(66), 2020.

[17] R. Roozendaal, R. E. Mebius, and G. Kraal. The conduit system of the lymph node. *International immunology*, 20(12):1483–1487, 2008.

[18] R. Savinkov, A. Kislitsyn, Watson D. J., R. van Loon, I. Sazonov, M. Novkovic, L. Onder, and G. Bocharov. Data-driven modelling of the FRC network for studying the fluid flow in the conduit system. *Engineering Applications of Artificial intelligence*, 62:341–349, 2016.

[19] A. A. Tomei, S. Siegert, M. Britschgi, Luther S. A., and Swartz M. A. Fluid flow regulates stromal cell organization and CCL21 expression in a tissue-engineered lymph node microenvironment. *J. immunol.*, 183(7):4273–4283, 2009.

[20] A. Tümer, N. Öztürk Demir, C. Basar-Eroglu, and A. Noyan. Spontaneous contractions and stretch-evoked responses of isolated lymph nodes. *Journal of Muscle Research and Cell Motility*, 4(1):103–113, 1983.

[21] G. N. Watson. *A Treatise on the Theory of Bessel Functions*. Cambridge University Press, Cambridge, England; The Macmillan Company, New York, 1944.